Linking plasma formation in grapes to microwave resonances of aqueous dimers

3 authors, including:

Hamza Khan Khattak
Trent University
5 PUBLICATIONS   **22** CITATIONS

Aaron D Slepkov
Trent University
79 PUBLICATIONS   **1,299** CITATIONS

Some of the authors of this publication are also working on these related projects:

Project   Multiple-choice testing and Integrated Testlets   View project

Project   Total Synthesis & Bioorganic, Pharmaceutical and Medicinal Chemistry   View project

Linking plasma formation in grapes to microwave resonances of aqueous dimers

Hamza K. Khattak[a], Pablo Bianucci[b], and Aaron D. Slepkov[a,1]

[a]Department of Physics and Astronomy, Trent University, Peterborough, ON, Canada K9L 0G2; and [b]Department of Physics, Concordia University, Montreal, QC, Canada H4B 1R6

The sparking of cut grape hemispheres in a household microwave oven has been a poorly explained Internet parlor trick for over two decades. By expanding this phenomenon to whole spherical dimers of various grape-sized fruit and hydrogel water beads, we demonstrate that the formation of plasma is due to electromagnetic hotspots arising from the cooperative interaction of Mie resonances in the individual spheres. The large dielectric constant of water at the relevant gigahertz frequencies can be used to form systems that mimic surface plasmon resonances that are typically reserved for nanoscale metallic objects. The absorptive properties of water furthermore act to homogenize higher-mode profiles and to preferentially select evanescent field concentrations such as the axial hotspot. Thus, beyond providing an explanation for a popular-science phenomenon, we outline a method to experimentally model subwavelength field patterns using thermal imaging in macroscopic dielectric systems.

microwave photonics | dielectric resonators | plasma ionization | hydrogels | morphology-dependent resonances

It is a truth universally acknowledged that a pair of grape hemispheres exposed to intense microwave radiation will spark, igniting a plasma. This parlor trick has become a mainstay of science-fair projects and popular-science blogs (1), as well as online videos for over two decades (a YouTube search for "grape plasma microwave" will show numerous results for the phenomenon). The phenomenon is invariably demonstrated with a grape, cut in half with a thin line of skin left to bridge the two hemispheres and irradiated in a household microwave oven for a few seconds, sparking a plasma from the skin bridge (Fig. 1A). Numerous online videos that demonstrate this effect in an identical arrangement have garnered millions of views. While no formal literature exists to offer a physical explanation for this phenomenon, several popular-science sources online presume that the pair of hemispheres act as a short dipole antenna of sorts (2), with the conductivity of the wet and ion-rich skin bridge being a key component.

While an explanation based on surface conductivity is a priori plausible, we present evidence that the effect has a bulk optical origin. Specifically, that the effect is a result of aqueous dielectric objects displaying morphology-dependent resonances (MDRs) at microwave frequencies. MDRs are synonymous with Mie resonances, which describe the near-field effects of resonant interactions of light with wavelength-scale objects (3, 4). The objects can be conductive or dielectric and absorptive or transparent, depending on the complex dielectric permittivity of the material. Research into pairs of conducting particles at nanoscales and microscales has shown a ubiquity of hotspots at the point of contact (5). Such surface plasmon resonances (SPRs) are localized to the surface (6, 7) and have been used to probe or excite molecular species that are too small to resolve by traditional optical methods (8, 9). The fact that nonabsorbing, nonconductive dielectrics can form MDR hotspots has garnered considerable recent attention (10–14).

In this article, we present methods for studying Mie resonances in absorbing dielectrics in the microwave regime. With thermographic studies, we offer a low-tech method for experimentally measuring internal and evanescent near-field electromagnetic concentrations with subwavelength resolution. We combine these methods with finite-element simulations to show progressions from isolated resonances to coupled-resonator supermodes in aqueous dimers. The hotspots formed represent superfocusing on the order of $\lambda_0/100$. With these tools, we provide a detailed description and explanation of plasma formation from fruit dimers in a microwave oven, as well as opening a sandbox for the study of nanocluster photonics using absorbing dielectrics.

The Formation of Plasma from Aqueous Dimers

The "grape plasma" phenomenon is currently restricted in the lay media to grape hemispheres, usually connected by a strip of skin. Naturally, previous explanations for the phenomenon have invariably involved the roles of the skin and of the open wet surface in forming the plasma. However, we find that neither of these components are essential to the formation of the plasma. The phenomenon is exemplified in Fig. 1A and Movie S1. A close viewing of Movie S1 shows that the plasma is initially formed "under" the skin-bridge, toward the hemisphere volume, rather than being formed at the open end and ejecting away from the dimer. Second, as shown in Fig. 1B and Movie S2, whole (uncut)

Significance

In a popular parlor trick, plasma is created by irradiating grape hemispheres in a household microwave oven. This work ties the source of the plasma to microwave photonic hotspots at the junction of aqueous dielectric spherical dimers. We use a combination of thermal-imaging techniques and computer simulations to show that grape-sized fruit and hydrogel beads form resonant cavities that concentrate electromagnetic fields to extreme subwavelength regions. This is enabled by the large dielectric susceptibility of water at microwave frequencies. Furthermore, the absorptive properties of water are key to washing out complex internal modes and for allowing the evanescent hotspot build-up. Our approach to microwave resonances in high-dielectric materials opens a sandbox for nanocluster photonics research.
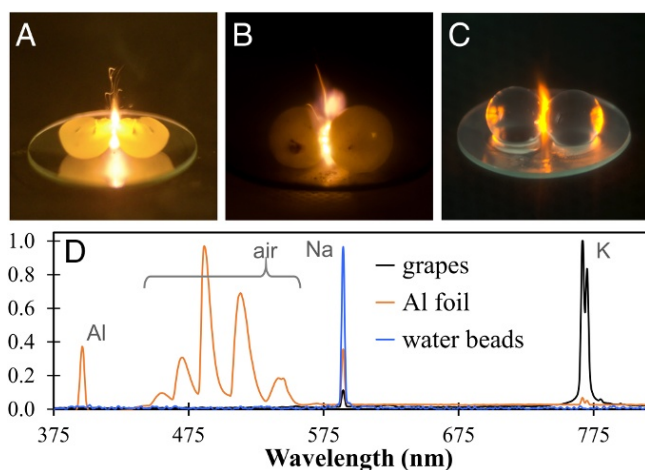
Fig. 1. (A) Plasma between grape hemispheres bound with a skin bridge in the traditional arrangement (Movie S1). (B) Whole grapes, weakly bound by their weight in a watch glass, also form plasma (Movie S2). (C) Skinless hydrogel beads are >99% water and also form plasma after a brief immersion in NaCl solution (Movie S3). (D) Normalized emission spectra collected through the microwave-oven door, demonstrating that the plasma is initiated by K and Na species in the grapes and by Na in the NaCl-soaked water beads. The distinct spectrum of plasma from aluminum foil is shown for comparison.

grape dimers also form a plasma despite having no bridge of skin. We deduce that the ubiquitous requirement for a skin bridge in most demonstrations serves as a means for keeping the hemispheres contacted as a dimer. As seen in Fig. 1 *A–C*, we achieve this in whole-sphere dimers by placing the objects on a small concave watch glass, where the objects are gently kept together by their weight.

To further demonstrate that this effect has a bulk optical origin—rather than a biophotonic origin that depends on the specific geometry, composition, and vasculature of grapes—we demonstrate plasma formation in NaCl-soaked sodium polyacrylate hydrogel beads, which are composed of nearly pure water (Fig. 1*C*). Interestingly, these beads tend to oscillate as they are irradiated (see frames at 1:50 in Movie S4). We are currently exploring these as driven oscillations arising from an elastic Leidenfrost effect (15).

Observing a piece of fruit burst into flames in a microwave oven is exciting and memorable. Consequently, much attention has previously focused on the plasma itself rather than the source of the sparking. As shown in Fig. 1*D*, emission spectra from grape plasma suggest that potassium and sodium species, abundant in the grape skin, are field-ionized by a strong concentration of electric field near the point of contact. The ions themselves are resonant with the driving microwave radiation and can evolve a cascade of ionization in the air, forming a microwave-heated plasma that grows and becomes independent from the dimer, as can be seen in high-speed Movie S4. However, the plasma itself is of secondary interest, as it ultimately only provides a thresholded indication of field concentrations. Since the sparking is often stochastic in nature, we turn to other characterization methods to elucidate the field concentration in aqueous spheres and dimers to confirm an explanation based on MDRs.

Internal Field Characterization

The best means of establishing that Mie resonances are involved in the creation of a dimer hotspot would involve the measurement of electric-field distributions both inside of the dielectric spheres and in the near field of the surface. The direct mea-

surement of such fields is extremely challenging, mainly because the hotspots are subwavelength. Fortunately, the fact that aqueous objects absorb at microwave frequencies can be exploited to allow thermal imaging to act as an indirect measurement tool for time-integrated field intensities. It is important to note that thermal maps largely represent surface temperatures and not internal temperature distributions (16). Thus, to image central temperature cross-sectional maps in whole-sphere-dimer experiments, the objects must be cut in half (either preirradiation or postirradiation) before imaging, as illustrated in Figs. 2*A* and 3.

In addition to thermal imaging, we use the finite element method (FEM) (COMSOL Multiphysics) to model the interaction of polarized 2.5-GHz microwave light with uniform absorbing spherical dimers of water and broadly confirm that the thermal-imaging maps reflect the anticipated field distributions from the plasma formation. The simulations yield an electromagnetic hotspot with the same behavior as the experimental hotspot present in the grape dimer system (Fig. 3 *H* and *I*). FEM simulations can also be coupled to heat-transfer calculations to obtain simulated thermal maps in such systems. These maps show good qualitative agreement with the experimental results (*SI Appendix*, Fig. S2). Detailed information on the simulation parameters, including thermal coupling, can be found in *SI Appendix*.
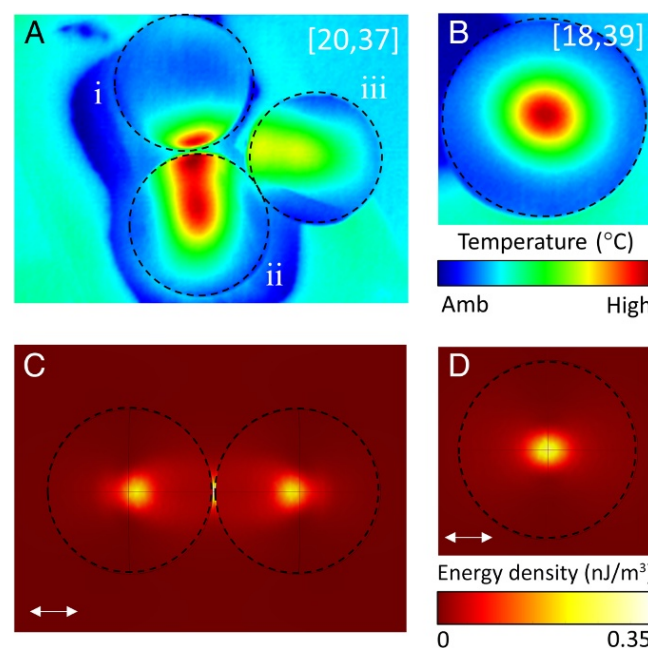

Fig. 2. Thermal maps of large 5.5-cm-diameter water beads. (A) The temperature distribution after 4-s irradiation of a hydrogel dimer showing the importance of acquiring an image from the flat section of interest. Object *i* is a whole sphere, showing only the hotspot on the surface near the point of contact; regions *ii* and *iii* are the postirradiation halved sister spheres to *i*, showing a more complex thermal distribution at the equatorial planes. (B) The temperature distribution of a postirradiation-halved large bead monomer, showing a well-confined radial mode that is hottest in the center. Thermal features outside of the marked regions of interest in *A* and *B* are reflections, spurious heating, or imaging artifacts from other surfaces in a plane below the spheres. The minimum and maximum temperatures that represent ambient and hot in the linear color scale are listed in square brackets. *C* and *D* are FEM simulations of geometries *A* and *B*, respectively, with 55-mm bead diameters and 1-mm bead separation. The arrows indicate the electric field polarization. Note the hotspot between the dimers in *C*. The "high" value in *C* is 0.35 nJ/m³ and 0.29 nJ/m³ in *D* for a 1-V/m input field.
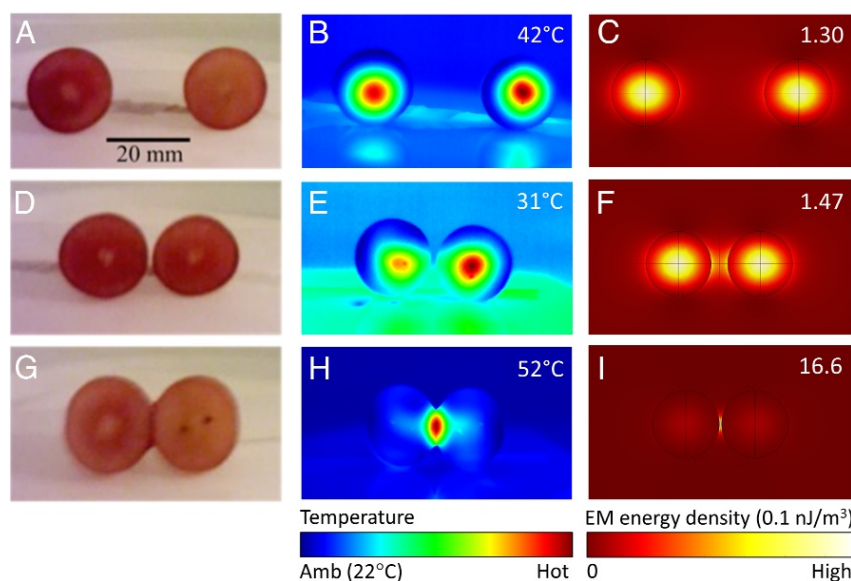
Fig. 3. Mode evolution in grape hemisphere dimers. *A*, *D*, and *G* show an optical image of the hemisphere arrangement. *B*, *E*, and *H* show the corresponding thermal images of the hemispheres/dimer obtained within 10 s after a 3-s irradiation. Maximum temperatures which define high in the color bar are reported to aid in qualitative comparisons among each column. The hotspot in *H* is of significantly higher temperature than those in *B* and *E*. *C*, *F*, and *I* show FEM simulations of the time-averaged energy density. The values in the top corner correspond to the high value on the color bar and are given in 0.1 nJ/m³ for an input field of 1 V/m. The low values are several orders of magnitude smaller in all cases and therefore effectively 0. The bead diameters are 16 mm and have separations of 20 mm (*C*), 4 mm (*F*), and 0.5 mm (*I*).

With thermal imaging, sparking is no longer desired, as it may add spurious heating effects. Consequently, thermal-mapping experiments use lower irradiation times, and hydrogel beads are hydrated with deionized water and not soaked in a saline solution. This allows us to measure the effect of bead size and separation on field-intensity maps in the system (Figs. 2 and 3). Live in situ thermal imaging shows qualitatively very similar structure to postirradiation imaging, as shown in Movie S5. Studying larger water beads, we note a well-defined central mode present in isolated spheres (Fig. 2*B*). This in itself is clear evidence of constructive interference, and therefore of a low-Q resonant cavity: With a penetration depth of ≈1.5 cm—smaller than the radius of the large beads—a simple model of absorption would be expected to yield a thermal pattern that is hotter near the surface, becoming less hot toward the center of the object as the microwave radiation is attenuated. The fact that water spheres of various sizes routinely yield the inverted pattern of a hot middle is thus evidence of optical resonance in isolated aqueous spheres. Moreover, when we control the orb separation within a dimer, we see a clear progression of mode structure from isolated resonators to a bonding mode with a concentrated hotspot, as shown in Fig. 3. We also observe that larger beads can simultaneously accommodate a supermode hotspot near the point of contact and a well-defined mode in their center (Fig. 2*A*). This is consistent with simulations (Fig. 2*C*), and in both cases, the internal modes become less marked as the central hotspot becomes stronger. As can be seen in Fig. 2*C*, central modes with little evanescent character also interact, moving slightly toward each other along the dimer axis.
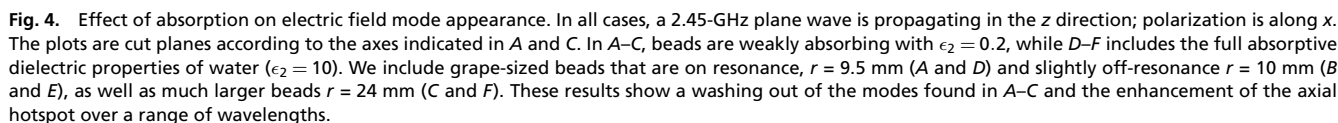
The Effects of Absorption

A key finding arising from our experiments and simulations is that similar field patterns persist across a wide range of dimer sizes. This is explained by the attendant absorption arising from the high imaginary component of the complex dielectric constant of water. At 2.45 GHz and 20 °C, $\tilde{\epsilon} = \epsilon_1 + i\epsilon_2 \approx 79 + i10$, with ϵ_1 most directly contributing to the index of refraction, and ϵ_2 most directly contributing to the absorption

coefficient* (17). When simulating a reduced absorption coefficient, the Q factor of the dimers is boosted, and a menagerie of complicated electromagnetic field modes are found inside the simulated beads, consistent with other reports for dielectric spheres (12). However, when the full absorptive behavior of water dimers is included, the wide array of modes found at lower absorption washes out, leaving relatively weak radially symmetric internal modes and an emergent hotspot localized to the proximal point of contact.

This behavior can be seen in Fig. 4, in which simulated field patterns in grape-sized and larger dimers are shown, both for the full dielectric behavior of water and for reduced-absorption objects of equivalent index of refraction. With lower absorption, hotspot resonances are sharp, and there is a large difference in mode strength between beads with small size differences. For example, simulated 9.5-mm-radius beads display an intense hotspot that is absent in 10-mm beads (Fig. 4 *A* and *B*). In the absorptive case, the mode strength remains more constant across a large size range. This indicates that formation of hotspots with absorption is a consequence of the broadening of the mode structure. The broadening results in more accessible intense hotspot-like modes, as well as homogenizing and suppressing higher-order internal modes. In a broad range of simulated sizes and separations, we find that absorptive dimers support a bright hotspot at the point of contact, even when no hotspot is found in simulations of negligibly absorbing equivalent dimers.

There are also trends with bead geometries. Generally, smaller beads at close dimer proximity favor a single hotspot between the two spheres. As beads are separated or increased in size, internal central modes better coexist with the dimer hotspot and become more apparent (Fig. 4*C*). The washing out of modes with increased absorption is exemplified by a broadening of resonance
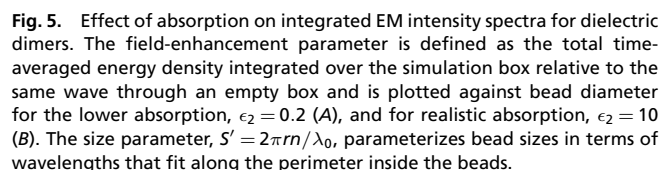
---

*Explicitly, the complex index of refraction is related to the complex susceptibility via $\tilde{n} = n + ik = \sqrt{\tilde{\epsilon}} = \sqrt{\epsilon_1 + i\epsilon_2}$, where n is typically referred to as the index of refraction and k, which is responsible for absorption, is referred to as the extinction coefficient. At 20 °C, we have $n = 8.9$ and $k = 0.56$.

Fig. 4. Effect of absorption on electric field mode appearance. In all cases, a 2.45-GHz plane wave is propagating in the *z* direction; polarization is along *x*. The plots are cut planes according to the axes indicated in *A* and *C*. In *A*–*C*, beads are weakly absorbing with $\epsilon_2 = 0.2$, while *D*–*F* includes the full absorptive dielectric properties of water ($\epsilon_2 = 10$). We include grape-sized beads that are on resonance, $r = 9.5$ mm (*A* and *D*) and slightly off-resonance $r = 10$ mm (*B* and *E*), as well as much larger beads $r = 24$ mm (*C* and *F*). These results show a washing out of the modes found in *A*–*C* and the enhancement of the axial hotspot over a range of wavelengths.

peaks, as can be seen in Fig. 5, which presents total integrated EM energy as a function of dimer bead size. As expected from a lower-Q resonator, an increase in absorption broadens the resonances and decreases their intensity in the bulk. This behavior thus supports the experimental observations that a microwave-induced hotspot is observed across a wide range of grape and hydrogel dimer sizes.

The functional dependence of the complex dielectric constant on temperature, frequency, and salinity provides an important avenue for future research. For example, at 2.5 GHz, the absorptive properties of water change more rapidly than does the index of refraction between the temperatures of 0 °C and 60 °C (17). Thus, details of resonant mode structure, including localized hotspots, may result in dynamic runaway or self-tuning processes arising from local absorptive heating. Such complex behavior may be observable with in situ live thermal videography (such as Movie S5). It is entirely possible that the dimer hotspot leads to localized heating that dramatically reduces absorption near the gap, but not in the bulk, yielding a positive feedback for hotspot intensification. The universality of the resonance behavior means that detailed thermographic observations of field dynamics in centimeter-scale aqueous structures can uniquely inform nanophotonic scattering processes that cannot at present be resolved at optical wavelengths.

Evanescent Hotspot Imaging with Thermal Paper

FEM simulations reveal a high-intensity field hotspot in the air gap within the dimer as the likely initiator of plasma in irradiated grapes. Because thermal-camera imaging relies on the effects of absorption in the object, the technique is insensitive to field distributions outside of the dimer. In an attempt to confirm both the hotspot in the air gap and the absence of evanescent field concentrations elsewhere around the objects, we use thermally activated paper that sharply darkens at a temperature of ≈85 °C (18). We use strips of thermal paper to monitor the outside temperature of individual spheres and dimers and to simultaneously create and monitor a gap within a dimer, as shown in Fig. 6. While the thermal paper can only indicate when a threshold of field intensity has been exceeded, and thus does not provide a continuous heat map like that from a thermal camera, these experiments provide key information about the near-field behavior of the aqueous dielectric objects.

When dimers are irradiated, they show a well-defined hotspot at the point of contact within an exposure time of 1–3 s. As seen

in Fig. 6 *A* and *E*, the hotspot appears to be most intense midgap between the beads, rather than at their surface. This behavior contrasts with simulations that show stronger evanescent fields near the surface when a significant gap is present (Fig. 3*F*). Thus, it is possible that thermal contact between the paper and the surface of the objects prevents a hotspot from being recorded on the shims closest to each surface. Nonetheless, simulations show significant field focusing spanning even significant gaps, which is confirmed with the thermal-paper experiments. We us two similar geometries to demonstrate this: First, as shown in Fig. 6 *A* and *B*, we can keep the dimer in contact by wrapping both
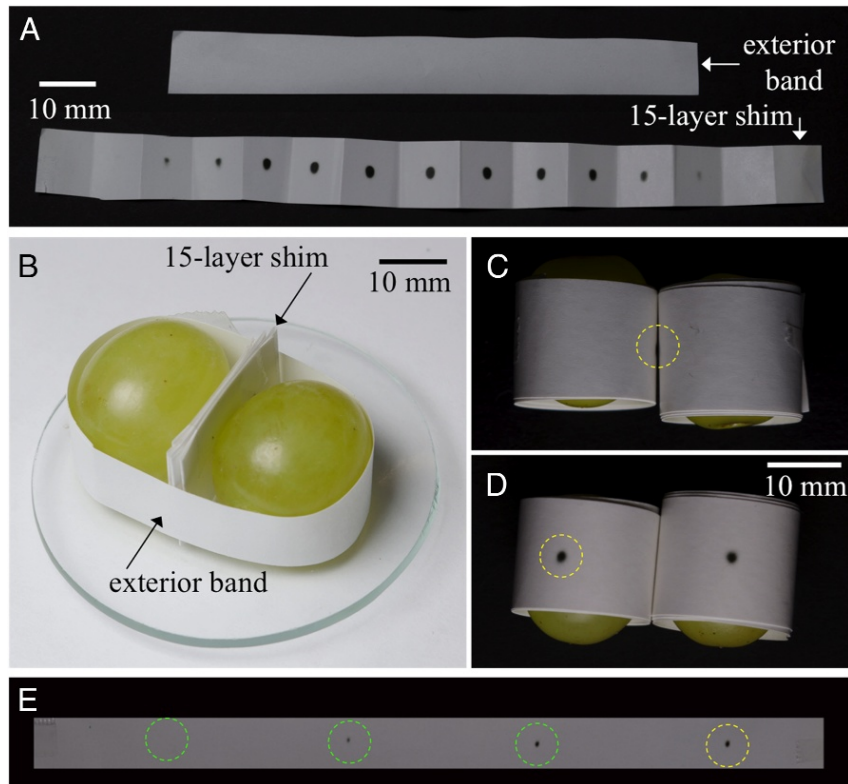

Fig. 5. Effect of absorption on integrated EM intensity spectra for dielectric dimers. The field-enhancement parameter is defined as the total time-averaged energy density integrated over the simulation box relative to the same wave through an empty box and is plotted against bead diameter for the lower absorption, $\epsilon_2 = 0.2$ (*A*), and for realistic absorption, $\epsilon_2 = 10$ (*B*). The size parameter, $S' = 2\pi r n / \lambda_0$, parameterizes bead sizes in terms of wavelengths that fit along the perimeter inside the beads.

Fig. 6. Near-field hotspot sectioning with 7.5-m-thick thermally activated paper. (*A* and *B*) The field intensity between two grapes is monitored with a folded 15-layered thermal paper shim, and the perimeter of the dimer is monitored with a band of thermal paper. (*C–E*) Alternatively, a band of thermal paper can be wrapped around each grape in a dimer to monitor the peripheral and gap field intensity. (*A*) A 3-s irradiation of the system shown in *B* yields a clearly defined hotspot in the 1.1-mm gap (shim), but no significant heating is observed on the periphery (exterior band). The gap sections closest to each object show a lower field intensity than at midgap, and the 15-section sequence implies a 3D thresholded field intensity map. (*C*) A grape dimer spaced by eight layers of thermal paper is irradiated for 2 s (*D*); the individual grapes have been rotated from the position in *C* to show an axial hotspot. (*E*) Unwrapped band from the left object in *D* showing a sectioning of the field intensity consistent with *A*. The yellow circle highlights the same physical position in *C–E*. The optical marks in *E* are smaller than 1.5 mm and represent extreme subwavelength ($\lambda_0/80$) thermal writing.

spheres together in a thermal paper band and then using a number of thermal-paper shims between the two spheres to form a fixed-length gap. We see a clear progression of intensity, with the highest intensity in the midgap shim. We can also individually wrap each bead in thermal paper (Fig. 6 *C* and *D*) and record the same progression, confirming high field strength through the entire gap (Fig. 6*E*).

Much of the interest in nanoplasmonics lies in the ability to create highly confined or intricately structured electromagnetic concentrations in subwavelength regions. Whether such hotspots are used for direct optical processing or surface patterning or are used to probe/excite volumes that are too small to access with typical diffractive approaches, the ability to confine light to particular subwavelength regions in exclusion of other nearby regions is of high technological interest. The optical writing demonstrated by the grape dimer on the thermal paper in the air gap represents a demonstration of resolution better than $\lambda_0/80$. With controlled excitation—in terms of fluence, time, and polarization—considerably smaller features will be achievable. While millimeter-sized thermal writing is not in itself a scientific advance, the demonstration of such control with microwave radiation in an absorbing dielectric is unexpected. The identified usefulness of absorbing dielectrics in this work broadens the range of potentially useful materials. More important, however, are the implications to nanophotonic technologies at the visible and UV wavelength scales, were semitransparent high-index natural dielectrics or metamaterials to be discovered.

Surface Geometry and Hollow Quail Eggs

Because the hotspot is observed for such a wide range of sizes and shapes, concerns may remain that the effect has an origin in the surface geometry and conductivity. While preexisting notions that the dimer is acting as a conducting short antenna are difficult to overturn definitively, we conduct an experiment that appears to preclude a "surface-only"-based explanation: We repeat the thermal-paper experiments with dimers of small quail eggs (minor axis diameter $\approx$ 24 mm). The eggs are individually wrapped in single-layer bands of thermal paper and placed in contact along their minor axis. After confirming that unmodified eggs display a hotspot at the point of contact, the eggs are evacuated through a hole at their apex and rebanded. Empty egg dimers do not reproduce the hotspot and, with longer irradiation, eventually display stochastic surface heating. When the eggs are refilled with water and rebanded, the dimer hotspot is reproduced (*SI Appendix*, Fig. S3). Visually, of course, it is impossible to discern whether the eggs are empty or filled with water, but a clear identification can be made from how they interact with microwave radiation. Thus, we eliminate surface effects such as conductivity as significant contributors to the formation of plasma from grapes in the microwave oven.

Summary

Through a combination of videography, FEM simulations, IR thermal imaging, and thermal-paper sectioning, we have shown that the popular-science phenomenon of forming plasma with grapes in a household microwave oven is explained by MDR

behavior. Grapes act as spheres of water, which, due to their large index of refraction and small absorptivity, form leaky resonators at 2.4 GHz. Mie resonances in isolated spheres coherently add when brought together such that the aqueous dimer displays an intense hotspot at the point of contact that is sufficient to field-ionize available sodium and potassium ions, igniting a plasma. This hotspot is shown to be spatially confined on subwavelength scales that approach $\lambda_0/100$.

Because water has a larger index of refraction, at 2.4 GHz, than any known dielectric at visible frequencies, it is possible to explore unique resonance geometries in the microwave regime that are currently inaccessible at visible wavelengths. Thus, this work is likely to open experimental opportunities for modeling nanophotonic resonance phenomena with scaled-up objects illuminated at microwave frequencies. More direct applications may include the design of passive omnidirectional wireless antennas, superresolution microwave excitation and imaging, and the invention of microwave-pumped dielectric spaser analogues (19).

1. Michaud PR (1994) Fun with grapes: A case study. Available at https://web.archive.org/web/20190130194653/http://pmichaud.com/grape/. Accessed February 2, 2019.
2. Muhlschlegel P (2005) Resonant optical antennas. *Science* 308:1607–1609.
3. Mie G (1908) Beiträge zur Optik trüber Medien, speziell kolloidaler Metallösungen. *Annalen der Physik* 330:377–445.
4. Kuwata H, Tamaru H, Esumi K, Miyano K (2003) Resonant light scattering from metal nanoparticles: Practical analysis beyond Rayleigh approximation. *Appl Phys Lett* 83:4625–4627.
5. Romero I, Aizpurua J, Bryant GW, García De Abajo FJ (2006) Plasmons in nearly touching metallic nanoparticles: Singular response in the limit of touching dimers. *Opt Express* 14:9988–9999.
6. Hutter E, Fendler JH (2004) Exploitation of localized surface plasmon resonance. *Adv Mater* 16:1685–1706.
7. Schuller JA, et al. (2010) Plasmonics for extreme light concentration and manipulation. *Nat Mater* 9:193–204.
8. Mayer KM, Hafner JH (2011) Localized surface plasmon resonance sensors. *Chem Rev* 111:3828–3857.
9. Willets KA, Van Duyne RP (2007) Localized surface plasmon resonance spectroscopy and sensing. *Annu Rev Phys Chem* 58:267–297.
10. Bakker RM, et al. (2015) Magnetic and electric hotspots with silicon nanodimers. *Nano Lett* 15:2137–2142.
11. Miroshnichenko AE, et al. (2015) Nonradiating anapole modes in dielectric nanoparticles. *Nat Commun* 6:8069.
12. Albella P, et al. (2013) Low-loss electric and magnetic field-enhanced spectroscopy with subwavelength silicon dimers. *J Phys Chem C* 117:13573–13584.
13. Zywietz U, et al. (2015) Electromagnetic resonances of silicon nanoparticle dimers in the visible. *ACS Photon* 2:913–920.
14. Devilez A, Zambrana-Puyalto X, Stout B, Bonod N (2015) Mimicking localized surface plasmons with dielectric particles. *Phys Rev B* 92:241412.
15. Waitukaitis SR, Zuiderwijk A, Souslov A, Coulais C, van Hecke M (2017) Coupling the Leidenfrost effect and elastic deformations to power sustained bouncing. *Nat Phys* 13:1095–1099.
16. Vollmer M, Mollmann KP (2011) Infrared thermal imaging: Fundamentals, research and applications. *Eur J Phys* 32:1431.
17. Wang J, Nguyen AV (2017) A review on data and predictions of water dielectric spectra for calculations of van der Waals surface forces. *Adv Colloid Interf Sci* 250:54–63.
18. Brother Mobile Solutions (2012) Guide to thermal paper: Selection, usage and archiving, Technical Report. (Brother Mobile Solutions, Broomfield, CO).
19. Oulton RF, et al. (2009) Plasmon lasers at deep subwavelength scale. *Nature* 461:629–632.